Standardized Approach for Assessing Wireless IoT Devices in Millimeter-Wave Industrial Work-Cell Channels

Mohamed Kashef, *Member, IEEE*, Kate A. Remley, *Life Fellow, IEEE*, Paritosh Manurkar, *Member, IEEE,* Joshua M. Kast*, Member, IEEE*, Iyemeh E. Uchendu, Robert D. Horansky*, Member, IEEE*, *Dylan Williams, Life Fellow, IEEE*, Matthew Simons, *Member, IEEE*, Michael Frey, Lucas Koepke, and Richard Candell, *Senior Member IEEE*

***Abstract*—We present a standardized, repeatable test approach that replicates key features of measured industrial environments in a fully-characterized hybrid test chamber. The hybrid chamber consists of an anechoic chamber along with movable metallic spheres that provide discrete reconfigurable multipath components. The chamber is characterized by a synthetic-aperture system providing a reference measurement that captures the non-idealities of the chamber along with the intended spatial multipath, completing characterization of the test environment. A key feature of our approach is the propagation of correlated uncertainties through to the final system response – including uncertainties specific to synthetic apertures such as cable bending due to scanning and inexact positioner locations. The uncertainty analysis provides statistically accurate knowledge of the environment, allowing separation of measurement errors from errors related to the device or system under test. We have also extracted three exemplar channels that capture key features of a work-cell-sized industrial environment from measurements made with the same synthetic aperture. Each exemplar channel presents different, realistic angular-diverse multipath challenges to a millimeter-wave internet-of-things device, subsystem, or active antenna under test. This allows engineers to evaluate their hardware designs in a physical, repeatable test environment and also facilitates future standardization of test methods for these and other millimeter-wave wireless devices.**

***Index Terms*—Exemplar channel; industrial internet of things; industrial wireless systems; millimeter-wave wireless; synthetic aperture; uncertainty analysis; wireless system.**

I. INTRODUCTION

STRONG interest in industrial internet-of-things (IIoT) applications has led to the recent development of channel models of the factory-floor environment [1], [2]. Such models include discrete and diffuse multipath components to capture, respectively, strong specular reflections (or clusters of reflections) from metal equipment and myriad weaker reflections that decay over time due to diffuse scattering. Channel measurements conducted in these environments are typically used to extract model parameters [3]. Knowledge of the uncertainty in the measurement allows separation of errors due to the measurement setup from those due to the device or antenna under test during design, and the overall assessment of device performance in certification testing [4], [5]. A key contribution of the present work is to provide representative reflective environments for such tests.

The extension of IIoT technology to millimeter-wave (mmWave) frequency bands is expected to decentralize decisions by use of independent “smart” nodes, monitor physical processes, and allow manufacturing tools to communicate and cooperate with each other in real-time. High reliability will be critical in these machine-to-machine (M2M) real-time manufacturing processes. Such M2M technology is anticipated, among other applications, for “work-cell”-sized environments consisting of a single or a few machines. The size of a work cell is typically on the order of 10 m per side or less [6]. By focusing on requirements for the work cell, rather than for the entire factory, M2M IoT device designs may be tailored to provide optimal reliability and performance [7]-[9]. This may also lead to improved channel models.

Evaluating mmWave IIoT devices and subsystems, including active antenna arrays, in representative highly reflective factory work-cell conditions allows system developers and hardware engineers to investigate new approaches such as adaptive wireless networks that can reconfigure on the fly to utilize adaptive beamforming. Providing such conditions in a repeatable over-the-air (OTA) test environment is the focus of our work. Our approach creates a physical, reconfigurable test environment that will provide specific, spatial test-channel

---

Manuscript submitted xx/yy/2026. This work was supported in part by the NIST Innovations in Measurement Science Program

M. Kashef and R. Candell are with the National Institute of Standards and Technology, Gaithersburg, MD 20899 USA (contact e-mail: mohamed.hany@nist.gov or richard.candell@nist.gov)

R.D. Horansky, L. Koepke, M. Frey and M. Simons are with the National Institute of Standards and Technology, Boulder, CO 80305 USA.

P. Manurkar and I. Uchendu are PREP Postdoctoral Research Associates at the University of Colorado, Boulder working at the National Institute of Standards and Technology, Boulder, CO 80305 USA.

K.A. Remley and D.F. Williams are retired from National Institute of Standards and Technology, Boulder, CO 80305 USA

J. Kast is a National Science Foundation Postdoctoral Research Fellow at the National Institute of Standards and Technology, Boulder, CO 80305 USA.

conditions that are representative of challenging non-line-of-sight (NLOS) channels that may be encountered in a factory work cell. The “exemplar channels” that we replicate in the test chamber were extracted from measurements performed in an industrial environment.

At mmWave frequencies, correlation between components of uncertainty can become pronounced. For example, the frequency response of a bent cable is periodic due to the interference of forward waves and waves reflected at the bend. As another example, highly correlated element position errors in a beamforming antenna array will tend to increase sidelobe levels while random position errors will tend to be cancelled out. Incorporating correlations such as these in this work provides a more accurate uncertainty analysis than the typical root-sum-of-squares, which assumes all errors are uncorrelated.

We illustrate three exemplar channels that provide different yet realistic challenges to a spatially diverse mmWave IIoT device under test (DUT). For example, one exemplar channel provides two widely spaced angles of arrival that may be used to evaluate the ability of beamforming algorithms that identify and utilize one non-line-of-sight signal path while filtering out the other. Another exemplar channel presents several spatially diverse, discrete multipath components arriving at the receiver within a short time window that may induce inter-symbol interference at the receiver. Due to our limited chamber size, we primarily focus on providing known spatial multipath conditions as opposed to temporal multipath conditions. However, alternate methods exist for testing a DUT’s ability to decode a signal under multiple temporal conditions, whereas testing the spatial characteristics of a DUT is more challenging.

By use of our fully characterized test chamber, we assess the nonidealities in the physical reproduction of these exemplar channel models. Thus, we extend the work of [10]-[15] by providing reference measurements having a comprehensive, correlated uncertainty analysis in realistic, reflective channels to which DUT measurements may be compared.

Once implemented in our test chamber, the exemplar channels are characterized with a reference synthetic-aperture channel-measurement system whose spatial resolution and dynamic range exceed those of a typical DUT. Such a reference system can quantify intentional multipath reflections within the test chamber as well as unintended, non-ideal specular and diffuse multipath that may affect the performance of a DUT. In use, the reference system is replaced with the DUT. Understanding the characteristics of the channel *a priori* allows a user to compare expected DUT performance to that obtained in a physical OTA space. Knowledge of the non-idealities of the test environment is of particular interest when the end application leverages multiple spatial channel paths, as for multiple-input, multiple-output (MIMO) or beam-steering technologies. By use of the reference system, no assumptions are needed regarding the test environment.

Synthetic-aperture channel-measurement systems [16], [17] utilize a receive antenna element mounted to a positioner, which is scanned sequentially to acquire the complex channel response in locations typically spaced by half an electrical wavelength (λ/2) at the highest frequency of interest. The temporal and spatial characteristics of the channel may then be reconstructed in post processing. In our case, the receive antenna is mounted to a small robotic arm. This measurement system induces fewer reflections than many large-form-factor channel sounders and the cost of requiring a static channel.

The OTA testing of mmWave systems, specifically in anechoic chambers, is considered in the literature, for example, in [5], [10]-[14] and the references therein. The focus of these works, in general, is performance evaluation of 5G mmWave equipment in different scenarios including the assessment of various integrated antennas, multiple-input-multiple-output (MIMO) techniques, demodulation schemes, and beamforming performance. However, these studies have not considered replicating specific scenario environments inside test chambers and achieving a realistic angular-diverse test scenario that is reconfigurable and repeatable, with uncertainties on chamber characterization traceable to fundamental parameters.

In this work, we demonstrate the construction of a test chamber that can achieve the above requirements to allow for OTA testing of fully integrated mmWave wireless equipment in controlled, challenging, and realistic scenarios. The testbed and associated uncertainty analysis provide an effective framework for standardization of device testing. We provide results demonstrating the evaluation of angle of arrival (AoA) and error vector magnitude (EVM) under different exemplar channel scenarios, highlighting the practical usefulness of the approach.

In Section II, we discuss the test environment that creates our exemplar channels, the synthetic-aperture approach used in our channel characterization, the estimation of the key performance metrics angle of arrival (AoA) and error vector magnitude (EVM), and the estimated uncertainty in both the channel characterization and the metrics. In addition to common instrumentation-related uncertainties, we provide a discussion of uncertainties related specifically to synthetic apertures, including cable bending due to scanning and the potential systematic errors in the positions of the robotic arm that forms the array. In Section III, we discuss the identification of the exemplar channels based on measurements we made in an industrial environment and the clustering approach we use for the extraction of key channel features that may be represented by exemplar channels. In Section IV, we then present three exemplar channels that provide a range of spatial-multipath channel conditions. We compare the high-precision reference measurement (based on a 35 x 35 planar synthetic aperture) to a simulated phased-array DUT. We intentionally introduced a spatial offset in the physical location of the simulated DUT to study the consequence of positioning errors when comparing DUT measurements to reference measurements and illustrate that the reference system parameters can be tailored to identify non-idealities in the performance of the phased-array DUT. Section V presents our conclusions and future work.

II. REFERENCE-MEASUREMENT APPROACH FOR CHARACTERIZING HIGH-MULTIPATH ENVIRONMENTS

A. Hardware Setup

The NIST millimeter-wave, synthetic-aperture channel measurement system is capable of characterizing a variety of mmWave measurement scenarios, from 3D multipath channels to wireless hardware verification in controlled laboratory environments [16]-[19]. The system was designed to traceably bound all measurement uncertainties while maintaining correlations between components of uncertainty, as discussed in [17]. For characterizing the industrial work-cell environments shown here, the system was configured to operate over a wide frequency band (26 GHz to 40 GHz) in order to capture detailed delay characteristics of the channel, and with a dense aperture grid (35 x 35) in order to capture details of the spatial characteristics of the channel. When comparing the reference channel measurements to DUT measurements, the frequency range was reduced to 28.5 – 29.5 GHz to emulate a typical mmWave IoT device.

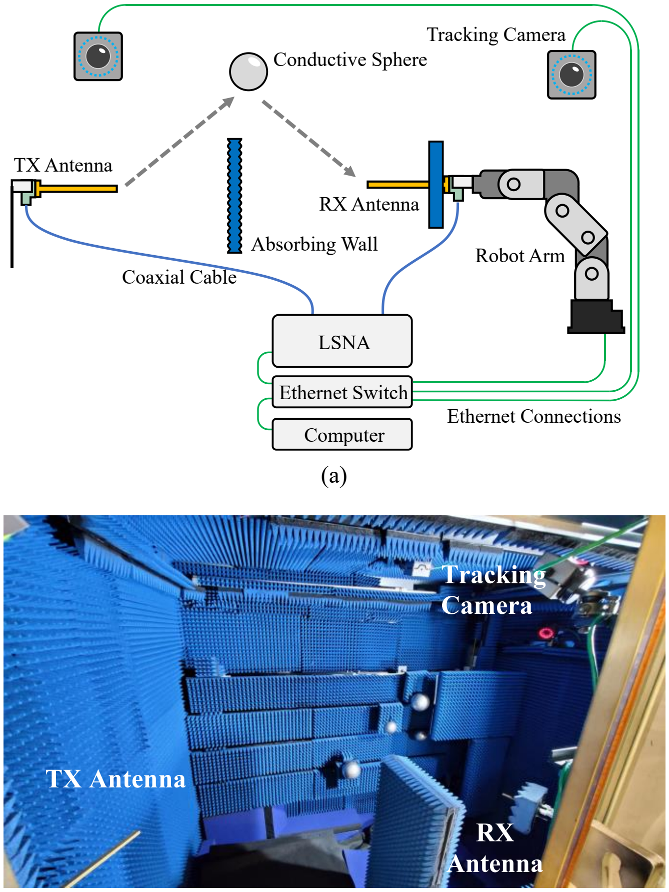

(a)

(b)

Fig. 1: (a) Diagram of the NIST synthetic-aperture system showing the transmit antenna, the robotic-arm positioner that forms the scanning synthetic aperture at the receiver, and the LSNA/VNA. A camera-based optical tracking system is illustrated at the top. The cameras image reflective markers placed in the measurement environment to track position uncertainty. (b) Hybrid anechoic/reverberation chamber consisting of movable reflective spheres, a small wall of RF absorber blocks the line-of-sight path between the TX and RX. The robotic arm that forms the synthetic aperture is located out of sight to the right of the photo.

The synthetic-aperture measurement system, illustrated in Fig. 1(a), consists of a fixed transmit antenna, a receive antenna mounted to a robotic-arm positioner that forms the synthetic aperture, and a vector network analyzer (VNA) or large-signal network analyzer (LSNA) to measure the static channel's complex impulse response. The robotic arm allows a variety of 3D synthetic-aperture scans with different geometries and polarizations. The arm that we used provides positional accuracy below 100 µm and repeatability in the tens of microns, as determined by an optical camera system that estimates the positions of the receive antenna as it scans.

For the present work, to characterize the exemplar channels created in our test chamber, we used WR-28 open-ended waveguide antennas for both the transmit (TX) antenna and the receive (RX) antenna. These antennas had 6.5 dBi gain, were linearly polarized, and had a 62°/104° beamwidth in the E/H planes. We did not de-embed the pattern of these broadband probe antennas prior to beamforming.

The LSNA was used to measure the transfer function of the channel with conventional scattering parameters, as would a standard VNA. The LSNA can also measure the amplitudes and cross-frequency phases of the forward and backward waves, which is useful for characterizing phased-array antennas or other active radiating devices. For an LSNA, the standard VNA scattering-parameter calibration is augmented with power and phase calibrations. These calibrations are traceable to fundamental parameters after propagating the uncertainties. This process supports NIST's goal of providing traceable spatial-channel OTA measurements. Specific measurement parameters for the results in the present work are provided in Table I.

TABLE I: VNA MEASUREMENT PARAMETERS

PARAMETER	FIELD TEST	TESTBED
Frequency Range	26.5 GHz to 40 GHz	26.5 GHz to 29.5 GHz
Frequency Step Δf	2.5 MHz	5 MHz
VNA IF Bandwidth	2 kHz	100 Hz
VNA Output Power Level (nominal)	-10 dBm	+5 dBm
VNA Dwell Time	10 µs	0 µs
VNA Calibration Reference Planes	WR28 waveguide port of a 2.4-mm (f) coax-to-waveguide adapter	VNA front panel after de-embedding cable and coax-to- waveguide adapter at antenna fixture

The testbed depicted in Fig. 1 is composed of a shielded chamber lined with RF pyramidal absorbing material specified to have -35 to -38 dB attenuation for normal incidence in the 26 – 40 GHz frequency range. The synthetic-aperture system is placed within the chamber. The transmit antenna is positioned to the left in the photograph in Fig. 1(b) and the receive antenna on its positioning robot is located on the right. Within the chamber, metal spheres act as scattering reflectors to emulate specular-multipath conditions seen in industrial environments. A small wall of RF absorbing material was placed in the middle of the chamber to ensure that only NLOS paths exist between the TX and RX antennas.

B. Synthetic-Aperture-System Analysis Approach

The synthetic aperture scans a single antenna element over an array of positions. In our case, this is a planar array that is generally oriented to face the incoming fields created by a multipath channel. In post processing, the fields from a wide range of angles of incidence are recreated by processing the measured incident fields with respect to angles. The incident field in the test volume from the direction (θ, φ) is calculated using the plane-wave expansion

$$S_{BF}(\theta, \phi, f) = \frac{1}{\sum_n W_n} \sum_n W_n S_n(f) e^{-j(k(f) \cdot r_n(\theta, \phi))}, \quad (1)$$

where n corresponds to each aperture element, W_n is a tapering weight at each aperture element, S_n is the measured S_{21} value at each aperture element, and $e^{-j(k(f) \cdot r_n(\theta, \phi))}$ is the steering vector such that $k(f)$ is the wavenumber as a function of frequency and $r_n(\theta, \phi)$ is the relative propagation distance of the nth element for a given azimuth θ and elevation ϕ. Without loss of generality, single polarization is considered in the present work, as discussed in Section II.D.2 and the Conclusion.

The delay resolution of the channel measurement is equal to the reciprocal of the synthesized bandwidth. For our configuration, with $f_{\min}$ = 26.5 GHz and $f_{\max}$ = 29.5 GHz, the total frequency extent is 3 GHz. Thus, the delay resolution Δt is equal to 0.33 ns. On the other hand, the maximum unambiguous delay extent, T = 200 ns, is the reciprocal to the frequency step, Δf = 5 MHz.

For the results shown here we used a square 35 x 35 planar aperture with 3.75 mm spacing between the spatial sample points, where 3.75 mm corresponds to 1/2 wavelength at 40 GHz. To illustrate the method, we used a smaller subset of 11 x 11 aperture to represent an antenna array of a commercial device under test.

After coherently combining the transmission parameters $S_{21}(f, \theta, \phi)$ measured across the synthetic aperture, the result is the complex frequency response of beams pointing to azimuth-elevation angle pairs θ_m, ϕ_n for $\theta_{\min} \leq \theta_m \leq \theta_{\max}, \phi_{\min} \leq \phi_n \leq \phi_{\max}$. The desired pointing directions for the peak of the main beam are chosen systematically using the approach described in [17] such that all the beams overlap at the 3-dB beamwidth. The boresight, half-power beamwidth (two-sided, 3 dB beamwidth) at 28 GHz is 8.4° for the 35 x 35 array and 26.4° for the 11 x 11 array.

After coherently combining the product of measured S_{21} values and complex beamforming weights across all of the aperture's spatial samples, we utilize an inverse Fourier transform to transform the frequency domain data to the temporal domain. While the beamforming equation above operates in the frequency domain to isolate spatial directions, the temporal characteristics of the channel are reconstructed to evaluate multipath arrival times. Intuitively, once the array is steered to a specific θ_m, ϕ_n to collect the total frequency response for that direction, the result acts as a directional transfer function. By applying an inverse Fourier transform to this directional frequency response, we reconstruct the complex impulse response.

For a certain pair θ_m, ϕ_n, the complex impulse response may then be defined as

$$h(\theta_m, \phi_n, \tau) = \sum_{l=0}^{L-1} \alpha_l \delta(\tau - \tau_l), \quad (2)$$

where α_l is the complex linear gain for the lth component in the delay vector, τ_l is the path arrival time, L is the number of the arrival paths in the delay vector, and $\delta(\tau)$ is the Dirac function. Taking the magnitude-squared of this vector provides what we define as a "directional PDP," with an example shown in Fig. 2, where we present PDPs representing an 8.4° angular space for the 35 x 35 array. Two PDPs at different directions are presented illustrating different temporal characteristics and received power levels.

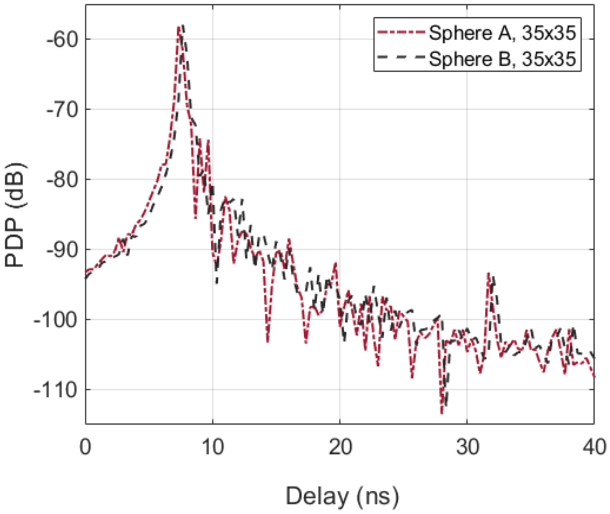

Fig. 2: Directional PDPs measured in the NIST IIoT testbed chamber by the 35 x 35 planar synthetic-aperture array for an exemplar channel having two discrete reflections arriving at the receiver from widely spaced angles of arrival. This exemplar channel is discussed further in Section IV.B.

We define the power associated with the path loss for this directional PDP, in decibels, as

$$P(\theta_m, \phi_n) = 10 \log \sum_{l=0}^{L-1} |\alpha_l|^2. \quad (3)$$

For the EVM results we show, we average the path loss (in linear values) across the bandwidth of the modulated signal of interest. For the heat maps, we average across a 100 MHz bandwidth. In both cases, the averaged results are then converted to decibels and denoted as a negative-valued "average gain."

This approach allows the development of "heat maps" that represent the spatial characteristics of the power in the received signal as a function of azimuth and elevation. Such a heat map is illustrated in Fig. 3(a), where one of the three exemplar channels discussed in Section IV has been measured by the 11 x 11 planar synthetic aperture in the IIoT testbed chamber. Areas of red indicate stronger reception paths from reflections off of the spheres, and blue-colored regions indicate locations where reflections are not present, or where signals are attenuated by the RF-absorbing material of the chamber. Note that the areas of strong reflection are not discrete points. The spheres are not ideal reflectors and the synthetic-aperture technique is able to capture effects such as angular spreading. Note also that the sidelobes of the synthetic aperture can introduce artifacts, which is why we limit the analysis range to ±90° in azimuth and elevation.

Figure 3(a) also shows that there are several unintentional reflections from the non-ideal anechoic material, fixtures and other material within the chamber. This represents a major advantage of the synthetic-aperture approach: non-idealities in the chamber setup can be visualized and corrected prior to measurements. Those not corrected can be included in the analysis of the DUT performance. Thus, we can separate chamber non-idealities from performance of the DUT. Figure 3(b) will be discussed in the next subsection.

C. Performance Metrics: Angle of Arrival and Error Vector Magnitude

Utilizing the spatial-channel response described in (3), as illustrated by the heat map in Fig. 3(a), we can estimate various performance metrics for both our reference measurement and simulated DUT. In the present work, we focus on two metrics that are often used in the design and test of a wireless DUT having an active antenna: First, the Angle of Arrival (AoA) of the strongest received signal or signals, which allows users to test the beamforming capabilities of their DUT. Second, the metric EVM allows users to test, among other things, error-correction capabilities in the presence of multipath.

1) Angle of Arrival

For the reference measurements, we determine the angle of arrival of the strongest reflections with a simple peak search over all azimuth and elevation pairs in the heat map. Recall that the synthetic-aperture beamforming algorithm accounts for the orientation of the aperture relative to the incoming multipath reflections. The grid over which the search is conducted corresponds to the angular resolution of the synthetic aperture, that is, 8.4° for the 35 x 35 array that we used or 26.4° for the 11 x 11. For the simulated phased-array DUT, we utilize the 11 x 11 array and then limit the peak search to a grid of points on the heat map that represent specific steering angles available to the DUT. The simulated DUT is described in more detail below in Section IV.A.

2) Error Vector Magnitude

To illustrate the use of the IIoT testbed with the EVM metric, we simulate an OTA-measured modulated signal by convolving the synthetic-aperture-derived channel with a computer-generated modulated waveform in post processing. It is important to note that our approach utilizes a post-processing convolution method to isolate the effects of the physical channel. This method specifically isolates channel-induced distortions, such as inter-symbol interference (ISI) from multipath, rather than hardware-induced impairments. Because the modulated signal is mathematically ideal, the resulting EVM does not include receiver-side IQ imbalance, phase noise, or frequency offsets, providing a raw evaluation of the physical test environment's impact on a hypothetical DUT.

The process for measurement and calculation of EVM is:

1. The VNA measures transmission parameter S_{21} at 35 x 35 = 1225 individual positions of the synthetic aperture.
2. The beamforming algorithm converts these S_{21} data into a channel response $h(t)$ at an angle of interest (here termed $h(t,\theta,\phi)$).
3. The ideal QAM waveform is computationally generated in the time domain (here termed $x(t)$).
4. We estimate how the QAM waveform would be affected by the channel by taking $z(t) = x(t) \circledast h(t,\theta,\phi)$ where $\circledast$ represents convolution, and $z(t)$ is an estimate of the distorted QAM waveform *as if* it had passed through the channel.
5. We calculate the EVM of the distorted QAM waveform. This EVM is computed with reference to the ideal waveform.

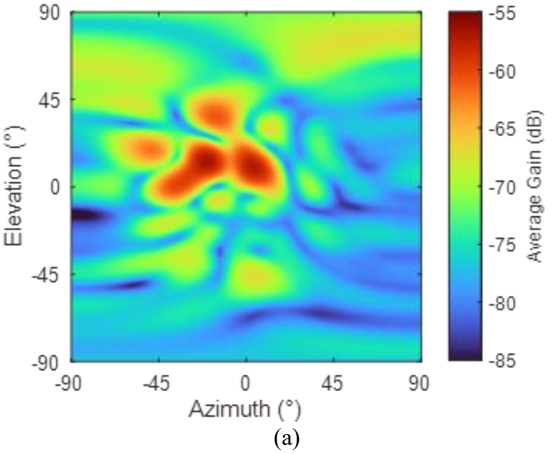

(a)

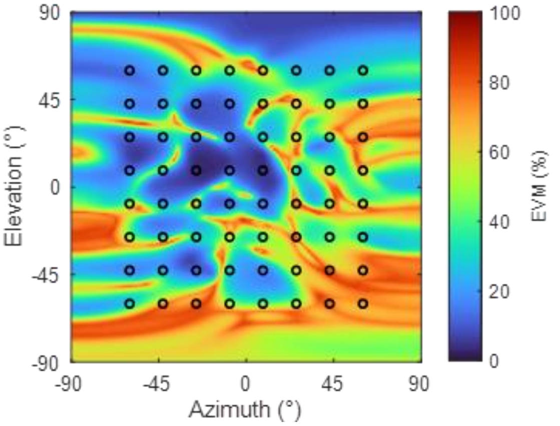

(b)

Fig. 3: (a) Beamforming result from the 11 x 11 synthetic-aperture measurement of an industrial exemplar channel created within the hybrid chamber. Areas of red indicate beamforming angles with high path gain. (b) EVM analysis result for beamforming data of Fig. 3(a). Areas of blue indicate low EVM, which may present viable paths for data communication. Figures originally from [20].

While not providing hardware distortion due to the generation and measurement of a real digitally modulated signal, this method illustrates well the capabilities of our testbed. While the results presented in Section IV would change with a real DUT, the method for comparing the reference EVM to the user-equipment's EVM remains the same. The convolution method presented in the steps above was discussed in more detail in [20].

For the work presented here, we use a fixed, repetitive 64-QAM waveform. The use of a repetitive signal allows us to perform reference measurements with the LSNA/VNA and, hence, apply NIST techniques for providing traceability in synthetic-aperture measurements. We generated 64-QAM waveforms at data rates of 50, 100, 200, 400, and 800 MSymbol/sec in order to study the effects of the chamber's frequency response on EVM. Each waveform consisted of an identical 808-bit data packet and a 32-bit cyclic redundancy check (CRC), for a total of 840 bits. The 840 bits were converted to 140 64-QAM symbols, which were filtered using a root-raised-cosine filter with a roll-off value of 0.35 and a filter length of 22 symbols. Waveforms were generated and saved in both time-domain and frequency-domain format for use in analysis.

We computed EVM by use of the standardized Baseline EVM Algorithm developed in [21]. The Baseline EVM Algorithm compares the two known symbol sequences at the intended constellation points and specified symbol-sampling times. EVM derived from this algorithm is based on the measurement of a repetitive signal $z(t)$ (with discrete spectrum $Z(\omega)$), given a finite-duration input signal $x(t)$ (with discrete spectrum $X(\omega)$.

Notably, the Baseline EVM Algorithm does not attempt to correct for the receiver-hardware-induced impairments, such as frequency offset or I/Q imbalance. This approach allows evaluation of the "raw" performance of a receiver before such impairments are corrected using signal-processing techniques. The result provides an evaluation of the DUT's hardware, as opposed to an evaluation of its ability to best decode the data carried by the signal. Because the algorithm is standardized, EVM may be compared across hardware types and labs.

To illustrate the application of the Baseline EVM Algorithm to our synthetic-aperture measurements, in Fig. 3(b), we show EVM results for the beamformed result of Fig. 3(a). Areas of blue in Fig. 3(b) are those of low EVM and represent paths by which a more successful transmission of data is anticipated. In Fig. 3(b), we have also overlaid an 8 x 8 grid representing a simulated phased-array DUT. This grid represents the limited set of discrete directions to which the DUT can steer. It is clear that the lowest EVM paths may not always be available to the phased-array antenna. The more complete knowledge of the multipath environment provided by the reference measurement may allow the development of improved beamforming algorithms or hardware designs.

D. *Uncertainty in Channel Characterization and Metrics*

Our goal is to provide realistic industrial channel responses with an uncertainty estimate with traceability to fundamental quantities [20]. An important aspect of the uncertainty analysis framework presented here is that we propagate errors induced by physical sources, such as the mechanical tolerances of VNA calibration standards, bending of cables during the synthetic-aperture scan and inexact locations of the robotic-arm positioner through to the final system response. This provides estimates for the uncertainty in complicated system responses such as power-angle-delay profiles or communication metrics such as error vector magnitude [22].

We implement our uncertainty analysis in the NIST Microwave Uncertainty Framework [23] by use of Monte Carlo simulations that also preserve the correlations that may exist between different sources of uncertainty. In this way, our approach to uncertainty evaluation yields more robust error estimates than the typical root-sum-of-squares method that may neglect correlated behavior between error sources.

Our methodology for evaluating the uncertainty in measurements made with our system includes components related to the measurement equipment, such as VNA calibrations and antenna responses, as well as setup specific components, such as cable movement or positioning errors during the scanning process.

1) *LSNA/VNA Calibrations*

The LSNA or VNA used to acquire the synthetic-aperture data is calibrated before and after every experiment. For the results presented in this paper, a short-open-load-thru (SOLT) WR-28 calibration was performed. Uncertainty in the dimensions of the physical artifacts used to calibrate the LSNA or VNA was propagated through to the final output of our Fourier processing. These uncertainties can be made traceable to fundamental quantities [24].

2) *Cable Movement*

During a synthetic-aperture measurement the probe antenna is moved through multiple spatial locations in the plane of the aperture. This probe is connected via a coaxial cable to the VNA and mounted to the robotic positioner. As the robot moves the probe to each position, this coaxial cable moves, flexes, and bends. These physical changes modify the electrical response of the cable in non-deterministic ways. Measurement of both polarizations requires performing a scan then rotating the antenna 90° and repeating the scan. We noted a significant cable relaxation time was required for accurate calibration and measurement [25]. Results in this work are presented for one polarization only.

3) *Probe Antenna De-Embedding*

In order to accurately characterize the wireless channel, it is necessary to de-embed the probe antenna response from our over-the-air measurements. This is especially important for the current work as we typically perform measurements over a wide bandwidth (13.5 GHz).

4) *Positioning Errors*

The locations of spatial samples in the synthetic aperture are used to calculate the steering vectors used in Fourier processing and determine the complex gain and pattern of the array. For example, the sample locations, and their errors (which can be made traceable to the meter), are used explicitly in beamforming since the separation between array elements determines the inter-element phase shift required to steer the beam to a given angle. In order to accurately account for positional uncertainty, we must explicitly track robot positions and use these data in our analysis.

If the antenna position errors were isotropic and uncorrelated, then the corresponding phase errors would be independent random variables that could cause a decrease in directivity (gain, for our purposes) of the array, and an increase in the variance of the deviation of the beam angle [25]. As well, exploratory analysis for robotic positioners has shown that correlated position errors can create noticeable spurious lobes in the beamformed array output. In the present work, we study the impact of correlated position errors on the AoA and EVM performance metrics.

To do this, we used an optical camera system that tracks the robot, antenna, and objects in the scene and provides accurate real-time position estimates. Our optical system utilizes a suite of 7 cameras, each with an approximate 168° field of view, mounted along the periphery of the measurement environment to take snapshots, at 30 or 180 frames per second, of markers placed on objects in the scene. Once calibrated, the camera system synchronizes the multiple snapshots and triangulates the locations of the markers to a 3D accuracy nominally on the order of 200 µm.

The position error estimated at each spatial sample of the planar 35 x 35 lattice is defined as the difference between the desired coordinates of the sample and the actual coordinates of the robot tip. An acceptable goal for position error is $\lambda/50$ which corresponds to 150 µm at 40 GHz. We next describe the extraction of the exemplar channels that we emulate in the IIoT testbed chamber.

In our work, we assessed position uncertainty by use of a commercial infrared camera system with reflectors attached to the waveguide antenna mounted on the robotic arm. The position of the antenna relative to the reflector was established with an infrared pen-probe system. The synthetic aperture's antenna orientation and position were tracked throughout the measurement with camera calibration occurring before every measurement set.

In addition, we developed a method to assess systematic errors in the positioning of the robotic arm by use of a NIST-developed 30 cm square calibration standard consisting of a 6 x 6 grid of infrared markers. The locations of the infrared markers were measured with a commercial coordinate measurement machine (CMM) with traceability to primary dimensional standards.

The 6 x 6 array of targets was held above a fixed mount by posts. We utilized seven post heights, each approximately 50 mm taller than the previous, to create a cube of points with calibrated locations. In postprocessing, the three-dimensional grid created by the optical measurements was aligned with the grid of the CMM coordinates to minimize spatial errors. The remaining differences between the CMM and optical locations in the three rectangular coordinates were then recorded to provide uncertainties in the positions of each antenna location in the synthetic aperture.

Spatial errors from each planar sample were incorporated into individual Monte Carlo calculations of angle of arrival to yield the distribution of expected results due to the correlated spatial errors. The uncertainties in angle are approximately 0.04 to 0.06 degree. Without accounting for positioning error in the camera system, the uncertainty estimate for the angle of arrival would have been up to an order of magnitude smaller. These errors are very repeatable for a given calibration of the camera system but change for every calibration.

III. EXTRACTION OF EXEMPLAR CHANNELS

From measurements made in an industrial environment with the 35 x 35 planar synthetic aperture, we extracted exemplar channels that provide key desirable features. To do this, we used a clustering technique to group the measurements according to specific key features encountered in the environment. We briefly describe the measurements and the clustering approach in [18]. We illustrate the extraction of the specific exemplars used to emulate an industrial work cell in the present work.

A. Millimeter-Wave Synthetic-Aperture Measurements in an Industrial Environment

Measurements were performed in the highly reflective Central Utility Plant at the Department of Commerce Boulder Laboratories in 2019. This environment consists of large boiler tanks, piping, and numerous racks of control hardware, as shown in the photographs in Fig. 4(a). The aisleway size in the utility plant is on the order of a factory work cell: w = 2 m by l = 6 m by h = 8 m, with a horizontal overhead tank approximately 4 m above the floor.

(a)

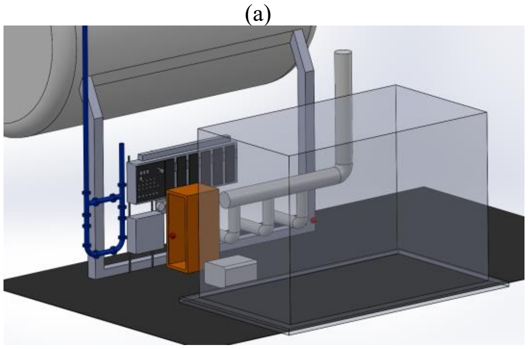

(b)

Fig. 4: The NIST Central Utility Plant where the measurements were conducted. (a) Aisleway with switch banks, pipes and large tank overhead. (b) Diagrammatic view showing the large equipment rack (in orange) simulating additional blockage in the aisleway.

An LSNA was placed in a small rack located between the transmit horn antenna and the synthetic-aperture receive array on the floor to minimize its invasiveness. We positioned the directional horn transmit antenna to point directly at the bank of switches and tanks shown in Fig. 4(a). It was oriented upward at an elevation angle of approximately 15°. Our synthetic-aperture receive array was oriented toward the switch bank as well, minimizing the direct line-of-sight component between the transmit and receive antennas. Note that the transmit antenna is around the corner and not visible in the photo of Fig. 4(a). In addition, the photo shows the synthetic-aperture array in its relaxed state, pointing downward.

To simulate a large piece of equipment, we placed a metal equipment rack in the utility plant environment (H = 127 cm, L = 56 cm, D = 67 cm), as illustrated in Fig. 4(b). The rack was placed directly in front of the transmit antenna, blocking some of the reflective switch bank. This configuration was intended to create disturbances to the angular characteristics of the channel caused by the additional reflections from the rack. Because this channel presented additional challenges to NLOS propagation between transmitter and receiver, we used it for the clustering and exemplar-channel extraction described in the following subsection.

B. Clustering Approach to Identify Exemplar Channels

In [18], we demonstrated a method to identify and characterize the spatial properties of wireless channels in industrial environments. The main idea of the approach is to cluster directional PDPs of the measured industrial channel based on channel features such that each group of directional PDPs with similar features is identified. Machine learning and dimensional reduction techniques were used because of the high dimensionality of the feature vectors and the complex mmWave channel behavior in various domains.

In [18], four sets of features were used to characterize a measured mmWave channel in an industrial environment. These four sets allowed the extraction of power-delay profile (PDP)-based, discrete-MPC-based, frequency-correlation-based, and diffuse-multipath-based features. The features were evaluated for each power-angle-delay profile (PADP) instance and are given in the Appendix.

A cluster of directional PDPs can then be represented by few PDPs that capture the most significant characteristics in this cluster. Thus, an exemplar represents a group of directional PDPs having similar features and within a specific range of similarity for the shape of their PDPs. Compared to the total number of PDPs, the number of exemplars is typically low and hence, testing a DUT over the exemplar PDPs allows the user to validate the DUT performance in a specific environment under different conditions without the need for exhaustive testing or on-site performance measurements.

An example is shown in Fig. 5, where clustering of measured synthetic-aperture data derived from measurements made in a utility plant is shown. All clustered directional PDPs are shown with the same color and the corresponding exemplars are marked by a specific symbol shape.

C. Simulated Phased-Array DUT

We illustrate the use of the hybrid chamber in evaluating the performance of a simulated mmWave IIoT DUT. In the following section, we will compare the DUT results to those of a reference measurement in specific exemplar channels. Whereas the reference measurement was performed with the 35 x 35 planar array described in Section II, the DUT's active antenna was based on a second set of planar synthetic aperture measurements with two significant changes. The DUT used an 11 x 11 planar synthetic aperture, having the approximate angular resolution of an 8 x 8 phased array (*i.e.*, both have ~26° beamwidth). Further, the simulated DUT was made more realistic by introducing a position offset representing a positioning error in the testbed chamber. The offset consisted of a shift back (away from the reflectors) behind the plane of the synthetic aperture for the reference measurement by 8.04 mm (where λ = 10 mm at 30 GHz), and a translational shift of 12 x 3.75 mm = 45 mm to the left of boresight (*i.e.*, the center of the 11 x 11 DUT planar array was shifted toward the chamber door by 45 mm).

The directions to which the simulated DUT could steer were limited to an 8 x 8 grid as illustrated in Fig. 3(b), unlike the synthetic-aperture measurements, which were beamsteered to create the heatmap in Fig. 3(a). To emulate a real device, we limited the range of the DUT's 8 x 8 grid to −60° to +60° in both azimuth and elevation. The choice of steering angle within a given exemplar channel was made by selecting the strongest received signal over all 64 discrete locations. Note that a real multiple-antenna device would likely use a more complicated beamsteering algorithm, but we use this simple method to illustrate the utility of a spatially diverse IIoT testbed.

In the following section, we compare reference measurements made with our 35 x 35 planar synthetic aperture to measurements of the same channel made with the simulated DUT (including the intentional positioning errors). Each of the three exemplar channels was derived from the measurements in the utility plant of Section III.A and is represented by the symbols extracted from the clusters of key channel conditions in Fig. 5.

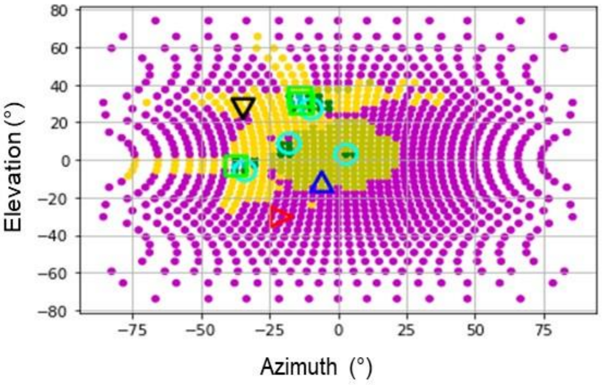

Fig. 5: Clustering of measured synthetic-aperture data derived from measurements made in a utility plant. Each of the four clusters, represented by a different color dot, corresponds to a set of channel features that characterize the measured industrial mmWave channel (see Appendix A). Exemplar channels that are representative of the key features in each cluster are indicated by the various symbols [18].

IV. EXEMPLAR CHANNELS AND DEVICE PERFORMANCE

We illustrate the use of the repeatable IIoT testbed chamber by assessing the performance metrics in Section II.C for the simulated DUT in Section III.C for measurements of three representative exemplar channels. Each exemplar provided different, realistic challenges for the DUT and was fully characterized with a reference measurement. As discussed in the Introduction, creating each exemplar channel with known accuracy allows users to test their DUTs in known conditions for debugging and performance verification.

Each exemplar channel was extracted by the clustering technique described in Section II.B and recreated in the hybrid chamber by moving reflecting spheres to various locations using the machine learning technique of [19].

The three exemplars presented below provide a set of unique, realistic challenges for design and test of wireless devices with active antennas operating in the 28 GHz band:

- Exemplar 1: Received signal significantly off boresight, with weak received power. *Goal: challenge the DUT's ability to efficiently beamform.*
- Exemplar 2: Two received signals with similar path gain arriving widely spaced in angle but closely spaced in time. *Goal: challenge the DUT's ability to identify the most robust path from among two channels having similar gain.*
- Exemplar 3: Received signal lies within a cluster of multipath. *Goal: challenge DUT's multiple-antenna systems in terms of robustness to ISI.*

For each exemplar channel, we determined the angles of arrival of the discrete multipath for both reference and DUT measurements. We also included a reference measurement made on the same 11 x 11 grid as the DUT, but without the position offset error. We then computed the EVM for both reference and DUT measurements. Because the EVM was computed in post-processing, we were able to assess performance over a variety of data rates, corresponding to several bandwidths of the 64-QAM waveform that we used. This illustrated the frequency dependent characteristics of the channels created in the hybrid chamber on device performance. In the interest of saving space, uncertainties are provided for the 35 x 35 reference measurement for Exemplar 3 only. Measured results from the three exemplars are presented next.

A. Exemplar 1: Single, Weak Non-Line-of-Sight Path

The first exemplar channel that we consider provides a relatively straightforward challenge for a beamforming device: identify a single NLOS reflection path that arrives from off-boresight of the RX antenna. We intentionally introduce noise into the received signal in post processing to challenge the DUT's ability to beamsteer and evaluate EVM for weak signals. This exemplar corresponds to the vertically-oriented red triangle in the cluster of magenta dots on the clustering map in Fig. 5. The desired and measured angles of arrival and the received power in the strongest received reflection for this exemplar are summarized in Table II.

TABLE II: CHARACTERISTICS OF EXEMPLAR 1 – CHANNEL WITH SINGLE, WEAK NON-LINE-OF-SIGHT PATH

Reflector	Desired	35 x 35 Ref. Meas.		8 x 8 DUT Meas.*	
	AoA (az/el)	AoA (az/el)	Gain (dB)	AoA (az/el)	Gain (dB)
Sphere A	-20°/ +30°	-19.9°/ +24.9°	−100.5	−25.7°/ +25.7°	-108.1

*8 x 8 discrete-steering grid based on 11 x 11 planar synthetic aperture with position offset.

To implement this exemplar in the hybrid chamber, we created the single, off-axis reflection by locating a reflecting sphere such that the signal arrived at the center of the receive array with an azimuth/elevation of approximately -20°/+30° using the machine learning technique of [19]. Note that in our

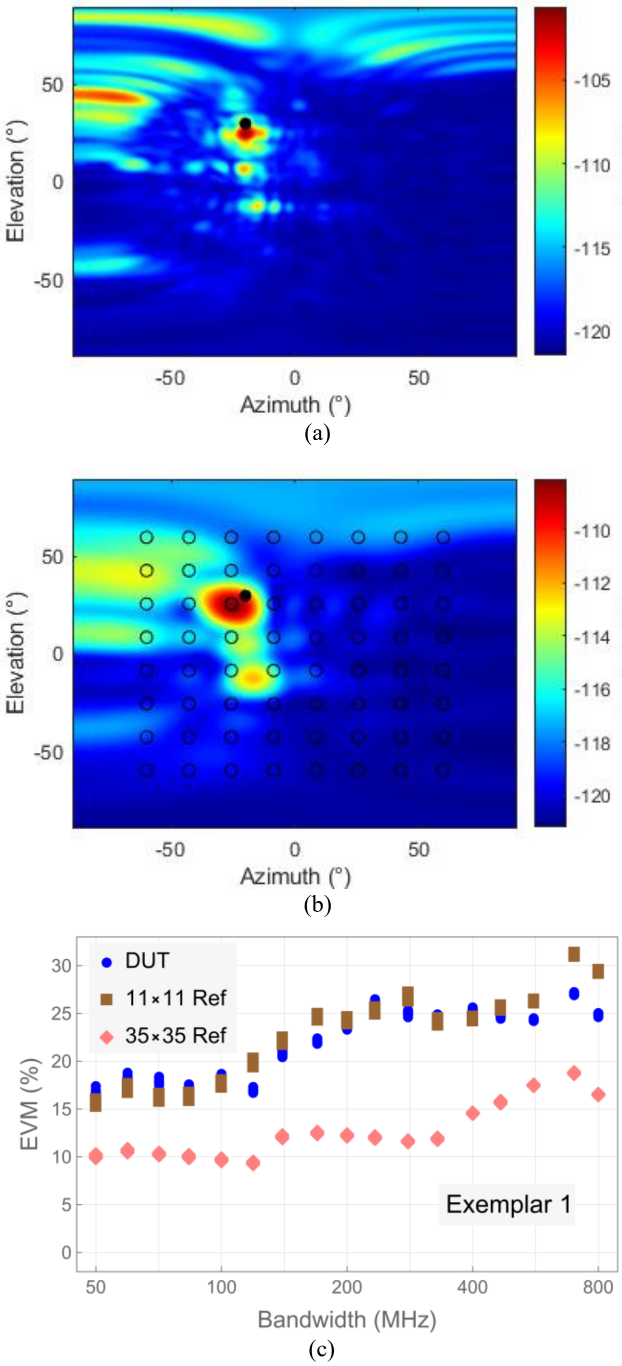

(a)

(b)

(c)

Fig. 6: Exemplar 1 *Single, Weak Non-line-of-sight Path*: (a) Heat map for the reference measurement made with a 35 x 35 synthetic-aperture planar array; (b) Heat map for the DUT measurement (consisting of an 11 x 11 planar array that includes an intentionally introduced position offset). Discrete steering locations for the simulated DUT's 8 x 8 phased array are shown by the black circles; (c) EVM computed for a range of 64-QAM modulation bandwidths for: the simulated DUT, an 11 x 11 reference (not limited to the DUT's 8 x 8 antenna locations), and the 35 x 35 reference measurement.

implementation of this exemplar, the elevation angle is positive instead of negative, as it was in the utility plant measurement. This is because the locations of the positioners holding the reflecting spheres in the hybrid chamber limit us to positive and slightly negative elevation angles. However, the positive elevation angle should present a similar challenge as the negative elevation angle would to a DUT's beamforming array.

1) *Angle of Arrival*

The heatmap corresponding to the channel power measured by the 35 x 35 reference array is shown in Fig. 6(a). The desired location of the AoA is shown by the black dot. The strong reflection from the single sphere can be seen in deep red at approximately -20°/+25° azimuth/elevation at the receive array. We see other, unintentional reflections represented by red and yellow shading. While these are weaker than the desired reflection, they physically do exist and may cause distortion or affect beamsteering. Thus, accurately characterizing them is a crucial part of evaluating a DUT in the test chamber.

Figure 6(b) illustrates the heatmap corresponding to the simulated DUT described in Section IV.A (based on an 11 x 11 array with a position offset 8.04 mm backwards and 45 mm to the left of boresight). The reduced spatial resolution corresponding to the 11 x 11 array is clearly seen by the spreading of the various incoming reflections. The discrete steering angles for the simulated 8 x 8 phased-array DUT are shown by the black circles. The strongest received signal obtained by the 8 x 8 array is at azimuth/elevation of approximately −26°/+26°. Note that the intentionally introduced position error (see Section III.C) has shifted the strongest reflection from the "desired" location indicated by the black dot.

We also performed an 11 x 11 reference measurement (not shown) without a position error, corresponding to what the DUT would ideally see without the position error or a restriction on its steering angles.

2) *Error Vector Magnitude*

We computed EVM over a range of modulation bandwidths corresponding to different data rates of the 64-QAM waveform, with results shown in Fig. 6(c). 11 repeat measurements are plotted. As expected, the lowest EVM values were obtained for the narrowest bandwidth of 50 MHz, corresponding to the least variation as a function of frequency across the modulation bandwidth (*i.e.*, the narrowest bandwidth provides the most "frequency flat" channel). These lowest EVM values were approximately 10.1% for the reference measurement and 16.8% for the DUT measurements. The significantly higher EVM for the simulated DUT may be attributed to the weaker received signal for the DUT due to the realistic, limited range of steering angles that we used for the DUT beamsteering implementation. The lower directivity associated with the 11 x 11 array for the DUT may also contribute to its higher EVM as compared with the 35 x 35 reference array.

As the channel bandwidth increases, the EVM increases as well, with maximum values of 18% for the reference measurement and 27% for the DUT measurement. The increase is not steady as a function of bandwidth due to the limited, discrete multipath in the channel. Further discussion is provided in Section IV.D.

Assessing DUT performance in weak, NLOS conditions from an off-boresight direction represents an important challenge to a DUT's ability to beamsteer and evaluate EVM for weak signals. For the case presented here, the limitation of an 8 x 8 antenna beamsteering grid resulted in decreased gain, with a corresponding increase in EVM. Such information is useful in the design phase.

B. *Exemplar 2: Two Widely Spaced, Similar-Gain Specular Reflections*

The second exemplar channel is intended to test a beamforming device's ability to identify the optimal channel when there are two possible strong NLOS paths. This exemplar illustrates why channel gain alone may not be the best choice for selecting the optimal channel within a reflective environment. A modulation-based metric such as EVM may be more appropriate because spatial interference (the constructive and destructive interference measured across the finite beamwidth of the RX antenna) may increase EVM, potentially degrading the communication link even when channel gain is relatively high [27].

In implementing this exemplar, we maximized separation in azimuth and elevation of the two specular reflections, providing two paths with similar channel gains with one had less non-ideal constructive and destructive spatial interference across the beamwidth of the antenna. This exemplar can be used to assess whether (1) a DUT can sufficiently spatially filter the two multipath channels to demodulate the signal and (2) the beamforming algorithm should use a metric other than channel gain to identify the more robust of the two channels. The exemplar in the next section will further stress the DUT's resilience to inter-symbol interference by providing multipath that is closely spaced in angle and unlikely to be spatially filtered.

This exemplar was modeled after the two green squares corresponding to the gold-colored cluster of dots in Fig. 5, although we increased the separation of the multipath components to evaluate coarse spatial filtering, as just mentioned. We implemented this exemplar in the IIoT testbed

TABLE III: CHARACTERISTICS OF EXEMPLAR 2 – CHANNEL WITH TWO WIDELY SPACED SPECULAR REFLECTIONS.

Reflector	Desired	35 x 35 Ref. Meas.		8 x 8 DUT Meas.*	
	AoA (az/el)	AoA (az/el)	Gain (dB)	AoA (az/el)	Gain (dB)
Sphere A	-46.2°/ +14.7°	-46.2°/ +14.7°	−55.5	-42.9° / +18.6°	-65.3
Sphere B	+16.0°/ -15.0°	+16.1° / -14.9°	-55.7	+8.6°/ −8.6°	-60.3

*8 x 8 discrete-steering grid based on 11 x 11 synthetic aperture with position offset.

Note: gray shading indicates AoA for selected channel.

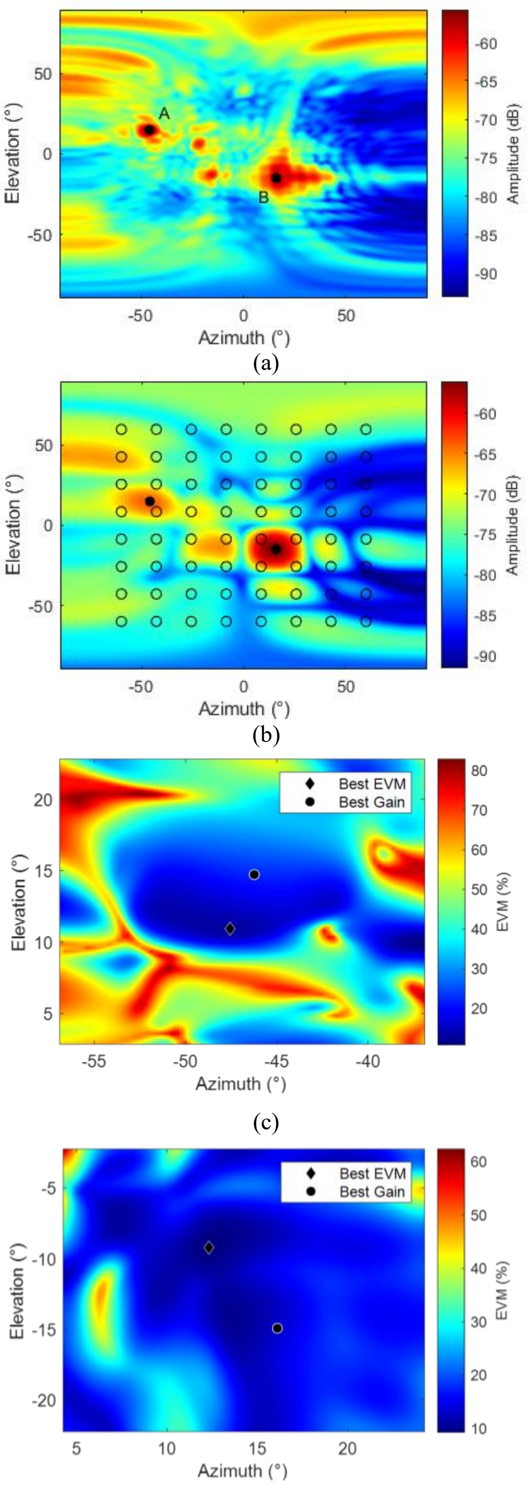

(a)

(b)

(c)

(d)

Fig. 7: Exemplar 2 *Two Widely Spaced Specular Reflections*: (a) Reference measurement made with a 35 x 35 synthetic-aperture planar array; (b) Heat map for the DUT measurement (consisting of an 11 x 11 planar array that includes an intentionally introduced position offset). Discrete steering locations for the simulated DUT's 8 x 8 phased array are shown by the black circles; (c) and (d) EVM computed from the 35 x 35 reference measurement over a narrower range of angles around Sphere A and B, respectively. Highest gain (circles) and lowest EVM (diamonds) are shown.

chamber using two reflecting spheres. As with the previous exemplar, we optimized the locations of spheres using the machine-learning technique in [19]. The desired and measured angles of arrival and the received power in the reflections from each sphere are summarized in Table III. Note that channel gain corresponding to the reference measurement is very similar for both spheres, while the DUT clearly shows higher channel gain for the Sphere B path. The reflections corresponding to Sphere B are shaded gray.

1) *Angle of Arrival*

The heat map corresponding to the 35 x 35 reference measurement is shown in Fig. 7(a). The desired locations of the AoAs are again shown by black dots and stronger received power is indicated by red shading. Non-ideal reflections are again seen as well. It is clear from the narrower region of high gain that the path corresponding to Sphere A would likely be more susceptible to spatial interference. That is, the communication link for the path corresponding to Sphere B would tend to be less susceptible to small position changes of the array, particularly when using a narrow, pencil-beam beamforming algorithm as we have for the 35 x 35 array.

Figure 7(b) shows the measured results for the wider-beamwidth simulated DUT with discrete steering angles (see Section III.C). As a simple demonstration device, this DUT's beamforming algorithm selects its steering angle by identifying the AoA of the strongest received signal, restricted to the black circles corresponding to the discrete locations to which the 11 x 11 array may steer. By inspection, the strongest AoA for the DUT corresponds to Sphere B, at an angle of +8.6°/−8.6° with a channel gain of −60.3 dB. The relatively wide beamwidth of this DUT provides a higher gain for the Sphere B path (as quantified in Table III), and so for this case path gain is an adequate metric. However, as discussed in the next subsection, for a DUT with a narrower beamwidth, a metric such as EVM may provide a more robust channel.

2) *Error Vector Magnitude*

As discussed above, in many cases, a channel that provides a wider spatial extent of low EVM values is desirable for robust communication. This effect, as emulated in the IIoT testbed chamber, is illustrated in Figs. 7(c) and 7(d), where we have computed EVM values from the 35 x 35 reference measurement in a narrow region surrounding the Sphere A and Sphere B paths that were shown in Fig. 7(a). For these plots, we again computed EVM using the convolution method described in Section II.C for a channel bandwidth of approximately 560 MHz.

The lower variation in EVM around the region of the Sphere B path shown in Fig. 7(d) indicates that a DUT array steered toward this channel may be more impervious to small spatial offsets as compared to the Sphere A path. This is supported by Fig. 2, where the path corresponding to Sphere B has a smoother power delay profile, making a DUT less likely to experience inter-symbol interference. To select the optimal (Sphere B) channel from this perspective, a beamforming algorithm that monitors channel conditions other than gain would be needed.

A comparison of EVM for the Sphere A and Sphere B paths is illustrated in Fig. 8, where we again computed EVM over a range of modulation bandwidths for 11 repeat measurements. With the channel corresponding to Sphere B, the DUT experiences a higher EVM than the 35 x 35 reference measurement and the corresponding 11 x 11 reference measurement. This may be expected by noting that the strongest reflection illustrated on the DUT heat map of Fig. 7(b) is located between the discrete beamsteering locations, reducing channel gain at the DUT and increasing EVM relative to the reference measurement.

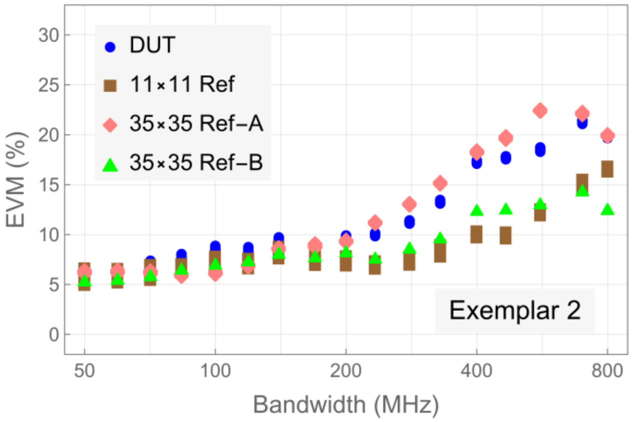

Fig. 8: EVM computed for a range of 64-QAM modulation bandwidths for: the simulated DUT, an 11 x 11 reference (not limited to the DUT's 8 x 8 antenna locations), and the 35 x 35 reference measurement computed for the Sphere A and Sphere B paths.

A key take-away from our measurements of Exemplar 2 is shown in the graph in Fig. 8, which shows the difference between the EVM for the Sphere A and Sphere B paths measured by the 35 x 35 reference system. For this case, the higher values of EVM for the Sphere A path confirm that a device with a narrower beamwidth may experience inter-symbol interference due to the narrow spatial characteristics of the channel. A beamforming algorithm that assesses more than just channel gain would allow such a DUT to select the Sphere B path even though it provides a lower received power. As well, Table III shows decreased gain for the DUT measurements, illustrating the limitation of an 8 x 8 antenna beamsteering grid, as we saw in Exemplar 1.

C. Exemplar 3: Many Diverse Angles of Arrival

Our third exemplar consists of four reflective spheres located well within the scanning range of the receive array in order to create dense, specular multipath. The angular separation of all spheres corresponds to a maximum separation on the diagonal of approximately 50°, which is significantly less than the previous exemplar, and is intended to test a receiver's immunity to ISI. As the most complicated exemplar, we provide uncertainties in AoA, path gain and EVM for the 35 x 35 reference measurement.

To implement this channel, we optimized the positions of four reflecting spheres to provide angles of arrival similar to those of the light-blue circles that exemplify the dark green dots in Fig. 5. The desired and measured angles of arrival and the path gain in the strongest received reflection for this exemplar are summarized in Table IV, with the strongest reflection shaded in gray. The corresponding standard uncertainties are small and are tabulated in Table V. These correspond to the standard deviation of 100 Monte Carlo simulations, as described in Section II.D.

1) Angle of Arrival

The Exemplar 3 heat map corresponding to the 35 x 35 reference measurement is shown in Fig. 9(a), with the desired locations for the four AoAs shown by the black dots. Fig. 9(b) shows the measured results for the simulated DUT with the positioning error. Measurements of an 11 x 11 array without positioning error were also made for comparison. The 11 x 11 reference measurement corresponds to what the DUT would ideally see if the DUT array was not restricted to the discrete steering locations.

The 35 x 35 reference measurement identifies the strongest incoming signal as coming from Sphere B at azimuth/elevation

TABLE IV: CHARACTERISTICS OF EXEMPLAR 3 – CHANNEL WITH MANY DIVERSE ANGLES OF ARRIVAL

Reflector	Desired	35 x 35 Ref. Meas.		8 x 8 DUT Meas.*	
	AoA (az/el)	AoA (az/el)	Gain (dB)	AoA (az/el)	Gain (dB)
Sphere A	−9.82° / +27.09°	−12.9° / +28.8°	−62.2	-8.6° / +25.7°	−72.6
Sphere B	−17.89° / +8.73°	−21.0° / +10.5°	−54.5	−25.7°/ −8.6°	−61.0
Sphere C	+2.9° / +2.9°	+2.4° / +4.2°	−56.5	-8.6° / +8.6°	−62.9
Sphere D	−34.01° / −5.81°	−37.9° / -7.1°	−54.9	-42.9° / -8.6°	−64.0

*8 x 8 discrete-steering grid based on 11 x 11 synthetic aperture with position offset.

TABLE V: UNCERTAINTY IN REFERENCE MEASUREMENT OF EXEMPLAR 3

Reflector	AoA Meas (az/el)	AoA **Std Dev W/O Pos Unc**** (az/el)	AoA **Std Dev With Pos Unc**** (az/el)	Gain Meas (dB)	Gain **Std Dev W/O Pos Unc**** (dB)	Gain **Std Dev With Pos Unc**** (dB)
Sphere A	−12.9°/ +28.8°	0.00° / 0.00°	0.06° / 0.06°	−62.2	0.02	0.04
Sphere B	−21.0°/ +10.5°	0.01° / 0.00°	0.05° / 0.05°	−54.5	0.02	0.03
Sphere C	+2.4°/ +4.2°	0.01° / 0.01°	0.04° / 0.05°	−56.5	0.02	0.03
Sphere D	−37.9°/ -7.1°	0.00° / 0.00°	0.05° / 0.04°	−54.9	0.05	0.07

** "W/O" and "With" refer to the standard deviation without and with including the component of uncertainty related to errors in positioning of the robotic arm, respectively.

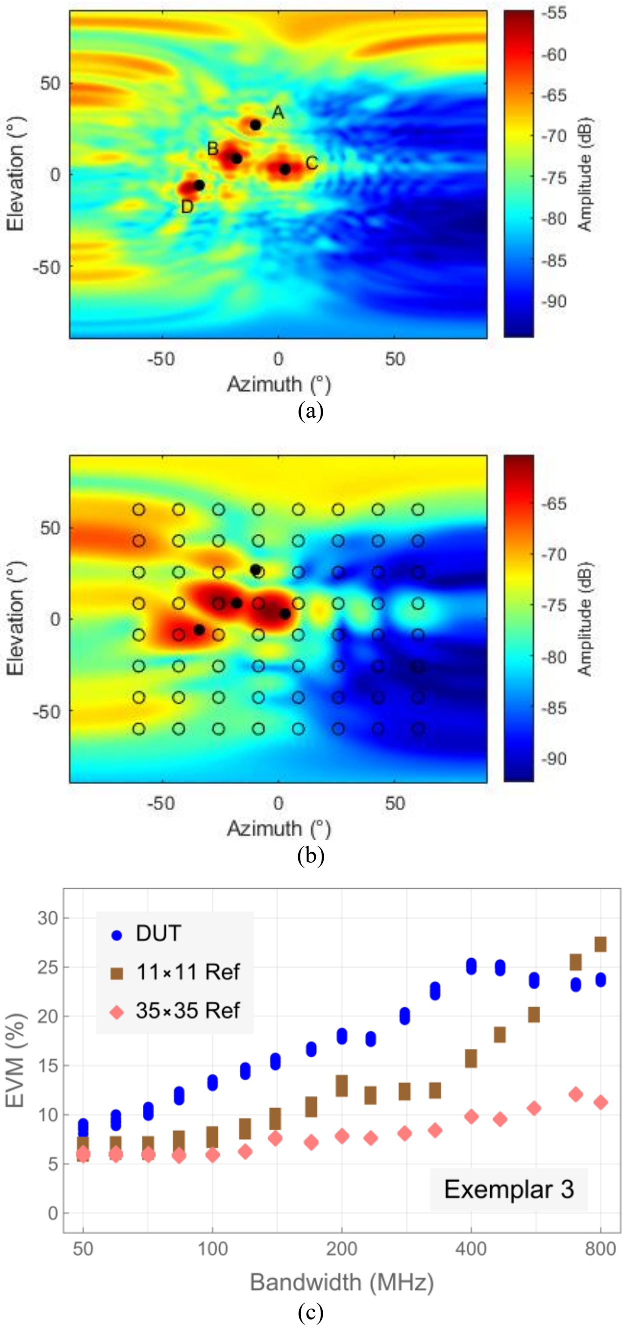

(a)

(b)

(c)

Fig. 9: Exemplar 3 *Many Diverse Angles of Arrival*: (a) Reference measurement made with a 35 x 35 planar array. Sphere B corresponds to the highest received signal; (b) DUT measurement (consisting of an 11 x 11 planar array that includes an intentionally introduced position offset). Discrete steering locations for the simulated DUT's 8 x 8 phased array are shown by the black circles; (c) EVM computed for a range of 64-QAM modulation bandwidths for: the simulated DUT, an 11 x 11 reference (not limited to the DUT's 8 x 8 antenna locations), and the 35 x 35 reference measurement.

of approximately −21.0°/+10.5° with a relative channel gain of −54.5 dB. We computed the standard uncertainties due to instrumentation and measurement-setup-related effects, including position uncertainty for the four measured reflections. For the azimuth and elevation, these range from ±0.04° to ±0.06°, as illustrated in Table V. Uncertainties on the gain range from 0.03 dB to 0.07 dB (for Sphere D). As a comparison, the standard deviation of the 11 repeat measurements is negligible to within two decimal places for azimuth, elevation and gain. This illustrates the importance of including other instrumentation and setup related effects on the estimate of our quantities of interest.

When the four strongest reflections measured by the simulated DUT (see Section III.C) at the locations denoted by the circles in Fig. 9(b) are compared to the reference measurement, we see that the DUT also identifies the strongest incoming signal as coming from Sphere B. This discrete phased-array AoA is −25.7°/+8.6° with a relative gain of −61.0 dB. As before, a more flexible beamforming algorithm could increase the received signal level by several decibels.

Note that the intentionally introduced position error in the DUT measurement causes a significant misalignment and, consequentially, weakening of the measured reflection from Sphere A, the sphere at the highest elevation angle. In fact, the DUT-measured AoA corresponding to this reflection is no longer located at the same discrete location as given by the 11 x 11 measurement. The misalignment in Fig. 9(b) could cause an error in the DUT's ability to identify the channel's main reflections. This illustrates the utility of using a well-characterized chamber for assessing DUT performance.

2) *Error Vector Magnitude*

We again computed EVM over a range of modulation bandwidths corresponding to different data rates of the 64-QAM waveform. Results are shown in Fig. 9(c), where 11 repeat measurements are plotted. The EVM for the reference measurement for the narrowest bandwidths is approximately 6%. For wider bandwidths, the EVM rises, reaching a maximum of approximately 12% at ~600 MHz.

The EVM of the DUT in this channel as a function of channel bandwidth is quite different from that in the previous two exemplars. The EVM is approximately 8% at our narrowest channel bandwidth of 50 MHz. It increases continuously and as a function of bandwidth to a value of approximately 25% at 800 MHz. These values are consistently higher than the ones for the previous exemplars. This is likely due to the intentionally created inter-symbol interference caused by the four spheres located in relatively close proximity. Note that the misalignment may be the cause of the higher EVM for the DUT as compared to an optimally aligned 11 x 11 array seen in Fig. 9(c).

We computed the standard uncertainty in EVM for the 35 x 35 reference measurement from 100 Monte Carlo samples, as described in Section II.D. Table VI illustrates results for three different modulation bandwidths. The values range from around 0.3% to over 2% depending on the sphere, with Sphere D having the highest values, likely because it is the farthest off boresight of the synthetic-aperture array.

3) *Reproducibility*

We end with a short note on reproducibility of this exemplar, and, by inference, the other exemplars in the testbed chamber.

TABLE VI: UNCERTAINTY IN EVM COMPUTED FROM 100 MONTE CARLO SAMPLES FOR VARIOUS MODULATION BANDWIDTHS

Reflector	50 MHz	200 MHz	560 MHz	800 MHz
Sphere A	0.82%	0.68%	0.55%	0.48%
Sphere B	0.80%	0.32%	0.38%	0.29%
Sphere C	0.37%	0.83%	0.28%	0.24%
Sphere D	2.03%	1.18%	0.69%	0.90%

We dismantled the TX antenna and RX array, then reassembled them in approximately the same locations at a later date. Figure 10(a) shows the heatmap and Fig. 10(b) shows the EVM for the DUT in this channel.

The heatmaps for the DUT measurements in Figs. 9(b) and 10(a) are quite comparable, with maximum channel gain values of -61.04 dB and -61.94 dB, respectively. However, the EVM values for the DUT, shown in Figs. 9(c) and 10(b), have changed significantly. This indicates that the spatial interference in the channel causes the EVM to vary as a function of location, as we observed with Exemplar 2. Note that a 5 mm offset in placement changes constructive to destructive interference at 28 GHz. Thus, reproducible placement of components in the chamber is necessary for comparing measurements made after physically reconfiguring the chamber. However, note that for a given setup the measurements are highly repeatable, as indicated by the overlap of the eleven repeat measurements in the graphs of EVM (see Figs. 6(c), 8, 9(c) and 10).

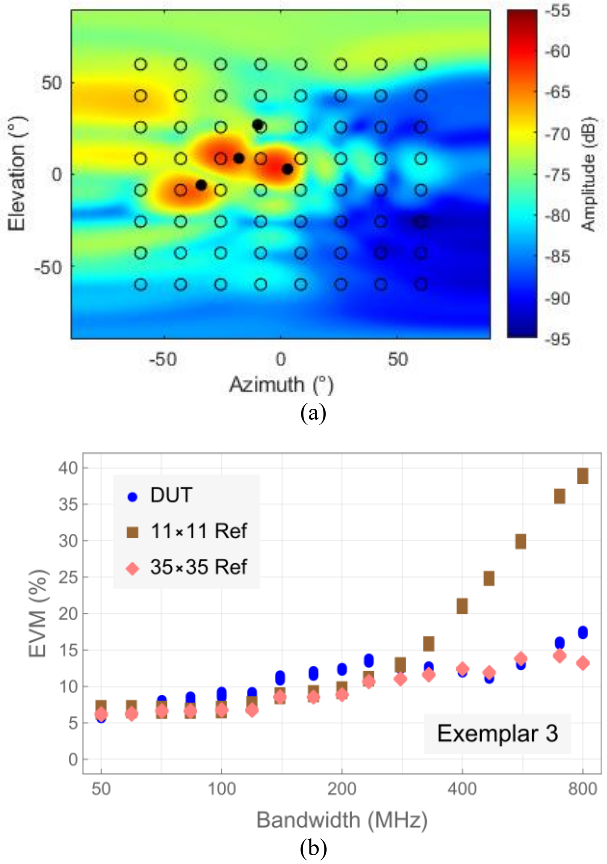

(a)

(b)

Fig. 10: Reproducibility of measurements of Exemplar 3 in the IIoT testbed chamber. (a) Heatmap for DUT (compare to Fig. 9(c)). (b) EVM computed for a range of 64-QAM modulation bandwidths for: the simulated DUT, an 11 x 11 reference (not limited to the DUT's 8 x 8 antenna locations), and the 35 x 35 reference measurement (compare to Fig. 10(a)).

The dense, specular multipath in Exemplar 3 was intended to test a receiver's immunity to ISI. The levels of EVM, ranging from 8 % to 25 % depending on the modulation bandwidth, were indeed significantly higher than for the previous exemplars. Thus, Exemplar 3 provides useful information for the design engineer in terms of spatial filtering and error correction.

D. *Discussion*

The results shown in Sections IV.A – IV.C align with what would be expected for the various challenges provided by each exemplar. For Exemplar 1, the lower signal-to-noise ratio for the DUT caused an offset in EVM as compared to the reference measurements. The reference and DUT EVM values covered a similar range, but the DUT had a higher value overall, which could be minimized, for example, with a more flexible beamforming algorithm.

For Exemplar 2, the limitations of a beamforming algorithm based solely on gain were illustrated. The reference measurement system illustrates that lower EVM may be found over a wider spatial extent for certain channels even when the path gain is similar or somewhat lower than other channels. This exemplar also tests the ability of a DUT to spatially filter one path from another.

Finally, Exemplar 3 illustrated that clustered multipath can create inter-symbol interference due to insufficient spatial filtering provided by the DUT's array.

Note that because we compute EVM in post-processing, we have been able to assess performance of a DUT over a variety of bandwidths of the 64-QAM waveform we used. This can give a design engineer insight into the frequency dependent behavior of a DUT having an active antenna, which can help improve the RF design. In practice, the DUT would reduce the modulation order (e.g., reducing from 64-QAM to QPSK) in a fixed-bandwidth channel. This would likely represent the deployment scenario but would test a different subsection of the receiver than the cases presented here.

V. CONCLUSIONS AND FUTURE WORK

It is important to have standardizable, repeatable, realistic factory-floor channel conditions for testing mmWave IIoT devices in spatially diverse, realistic, over-the-air conditions. The techniques illustrated here with the NIST IIoT testbed are intended to demonstrate the utility of a well-characterized chamber providing a set of spatially diverse test conditions. We extracted exemplar channels by clustering key performance metrics obtained from synthetic-aperture measurements made in an industrial environment whose spatial dimensions are on the order of a work cell. However, the chamber is spatially reconfigurable so that the user is not limited to the exemplar channels presented here.

The key to the testbed is defining a reference characterization of each physical channel with a full uncertainty analysis that accounts for correlations within error mechanisms. Creating each channel with known accuracy allows users to test their DUTs in known conditions for debugging and performance verification. By comparing the DUT's performance to what is expected for a channel with certain propagation conditions, an engineer can evaluate whether the DUT's hardware or software is performing as designed. This can be especially useful in assessing the performance of mmWave IIoT devices that have active antenna arrays, such as phased arrays or devices with multiple antennas, such as MIMO-type arrays. Chamber characterization also allows for the development of standardized testing protocols that can be verifiably reproduced in multiple laboratories.

In the work presented here, we prioritized creating spatially diverse channel conditions because techniques currently exist for testing the temporal characteristics of DUTs with channel emulators. Future work will implement machine learning to obtain a wider range of channel conditions, both temporal and spatial. We will also focus on comparing results for both polarizations after incorporating the significant cable relaxation time required for accurate calibration and measurement [25]. Finally, NIST is currently working on a 60 GHz implementation of the testbed as well.

ACKNOWLEDGMENT

The authors thank Peter Vouras, Sudantha Perera, Alec Weiss, Jeanne Quimby, Ben Jamroz, Damla Guven and Camillo Gentile for contributions to the NIST synthetic-aperture measurement system and analysis procedures.

APPENDIX A

The channel exemplar extraction approach is explained in detail in [18]. The features that are used to cluster the measured directional channels and determine the exemplars within each group are selected from four different metric domains, namely, the PDP-based, discrete multipath component (MPC)-based, frequency-correlation-based, and diffuse-multipath-based metrics. The selected features that we used for the work presented here are listed in Table VII.

TABLE VII: LIST OF FEATURES USED FOR EXEMPLAR EXTRACTION

Type	Feature
PDP-based	The total output power (dB)
	The mean delay (ns)
	The RMS delay (ns)
	The estimated noise level (dB)
Discrete MPC-based	The total power (dB) of the discrete MPCs
	The average SNR (dB)
	The SNR dynamic range (dB)
	The average K factor (dB)
	The mean delay (ns) of the discrete MPCs
	The RMS delay (ns) of the discrete MPCs
Frequency-correlation-based	The frequency offset (GHz) for input signal 26.5 to 40 GHz
	The frequency offset (GHz) for input signal 28 to 29 GHz
Diffuse-multipath-based	Number of threshold crossings above the noise threshold
	The estimated power of diffuse multipath (dB)
	The estimated ratio of diffuse power to noise power (dB)

REFERENCES

[1] "IEEE Standard for the Performance Assessment of Industrial Wireless Systems," in IEEE Std 3388-2025, vol., no., pp.1-67, 3 July 2025, doi: 10.1109/IEEESTD.2025.11071366

[2] "Study on channel model for frequencies from 0.5 to 100 GHz version 16.1.0", 2020, *[online] Available: https://www.etsi.org/deliver/etsi_tr/138900_138999/138901/16.01.00_60/tr_138901v160100p.pdf*

[3] R.Candell, K.A. Remley, J. Quimby, D. Novotny, A. Curtin, P. Papazian, G. Koepke, J. Diener, and M. Hany, (2017), Industrial Wireless Systems: Radio Propagation Measurements, Technical Note (NIST TN), National Institute of Standards and Technology, Gaithersburg, MD, [online], https://doi.org/10.6028/NIST.TN.1951

[4] "Technical Specification Group Radio Access Network; NR; Study on test methods," 3GPP, Sophia Antipolis, France, TR 38.810 v16.5.0, 2019.

[5] R. R. Barani, L. A. Bronckers and A. C. F. Reniers, "Integrated-Antenna Over-the-Air Testing for Millimeter-Wave Applications: An Overview of Systems and Uncertainty [Measurements Corner]," *IEEE Antennas and Propagation Magazine*, vol. 64, no. 5, pp. 97-110, Oct. 2022, doi: 10.1109/MAP.2022.3195469.

[6] K.B. Lee, R. Candell, H-P Bernard, Z. Pang, and I. Val, "Reliable, high-performance wireless systems for factory automation," *NIST Internal Report 8317*, Gaithersburg, MD, 2020.

[7] K. Montgomery, R. Candell, M. Hany, and Y. Liu, (2021), Wireless User Requirements for the Factory Workcell, Advanced Manufacturing Series (NIST AMS), National Institute of Standards and Technology, Gaithersburg, MD, [online], https://doi.org/10.6028/NIST.AMS.300-8r1/upd

[8] S. Sudhakaran, K. Montgomery, M. Kashef, D. Cavalcanti and R. Candell, "Wireless Time Sensitive Networking Impact on an Industrial Collaborative Robotic Workcell," in IEEE Transactions on Industrial Informatics, vol. 18, no. 10, pp. 7351-7360, Oct. 2022, doi: 10.1109/TII.2022.3151786.

[9] R. Candell, M. Kashef, Y. Liu and S. Foufou, "A SysML representation of the wireless factory work cell," *International Journal of Advanced Manufacturing Technology*, no. 40, pp. 104-119, 2019.

[10] S. G. Pannala, "Feasibility and Challenges of Over-The-Air Testing for 5G Millimeter Wave Devices," *2018 IEEE 5G World Forum (5GWF)*, Silicon Valley, CA, USA, 2018, pp. 304-310, doi: 10.1109/5GWF.2018.8516965.

[11] Y. Qi et al., "5G Over-the-Air Measurement Challenges: Overview," *IEEE Transactions on Electromagnetic Compatibility*, vol. 59, no. 6, pp. 1661-1670, Dec. 2017, doi: 10.1109/TEMC.2017.2707471.

[12] Y. Jing, M. Rumney, H. Kong and Z. Wen, "Overview of 5G UE OTA performance test challenges and methods," *2018 IEEE MTT-S International Wireless Symposium (IWS)*, Chengdu, China, 2018, pp. 1-4, doi: 10.1109/IEEE-IWS.2018.8400996.

[13] Y. Jing, H. Kong and M. Rumney, "MIMO OTA test for a mobile station performance evaluation," *IEEE Instrumentation & Measurement Magazine*, vol. 19, no. 3, pp. 43-50, June 2016, doi: 10.1109/MIM.2016.7477954.

[14] A. N. Uwaechia and N. M. Mahyuddin, "A Comprehensive Survey on Millimeter Wave Communications for Fifth-Generation Wireless Networks: Feasibility and Challenges," *IEEE Access*, vol. 8, pp. 62367-62414, 2020, doi: 10.1109/ACCESS.2020.2984204.

[15] K. A. Remley, "Next Generation Microwave and Millimeter-Wave Measurement Techniques," *2019 92nd ARFTG Microwave Measurement Conference (ARFTG)*, Orlando, FL, USA, 2019, pp. 1-1, doi: 10.1109/ARFTG.2019.8637248.

[16] A. J. Weiss et al., "Setup and control of a millimeter-wave synthetic aperture measurement system with uncertainties," in *Proc. 95th Autom. Radio Freq. Techn. Group Microw. Meas. Conf., 2020*, pp. 1–4.

[17] P. Vouras, et al., "Wideband Synthetic-Aperture Millimeter-Wave Spatial-Channel Reference System With Traceable Uncertainty Framework," *IEEE Open Journal of Vehicular Technology*, vol. 4, pp. 325-341, 2023, doi: 10.1109/OJVT.2023.3239617.

[18] M. Kashef, P. Vouras, R. D. Jones, R. Candell and K. A. Remley, "A Machine-Learning Approach for the Exemplar Extraction of mmWave Industrial Wireless Channels," *IEEE Open Journal of Instrumentation and Measurement*, vol. 1, pp. 1-15, 2022, Art no. 5500115, doi: 10.1109/OJIM.2022.3181309.

[19] M. Kashef, S. Perera, C. Nogueira, R. Candell, K. A. Remley and M. T. Simons, "A Deep Reinforcement Learning Approach for Automated Chamber Configuration Replicating mmWave Directional Industrial Channel Behavior," *2023 100th ARFTG Microwave Measurement Conference (ARFTG),* Las Vegas, NV, USA, 2023, pp. 1-6, doi: 10.1109/ARFTG56062.2023.10148878.

[20] J. M. Kast, et al., "Laboratory-Based Reference Channels for Millimeter-Wave Wireless Device Measurements," *2024 IEEE Conference on Computational Imaging Using Synthetic Apertures (CISA),* Boulder, CO, USA, 2024, pp. 01-05, doi: 10.1109/CISA60639.2024.10576590.

[21] IEEE Standards Association, "1765-2022 IEEE Recommended Practice for Estimating the Uncertainty in Error Vector Magnitude of Measured Digitally Modulated Signals for Wireless Communications," Nov. 2022.

[22] K. A. Remley, D. F. Williams, P. D. Hale, C. Wang, J. Jargon, and Y. Park, "Millimeter-wave modulated-signal and error-vector-magnitude measurement with uncertainty," *IEEE Trans. Microw. Theory Techn.*, vol. 63, no. 5, pp. 1710–1720, May 2015.

[23] D. F. Williams, NIST Microwave Uncertainty Framework, Beta Version. NIST, Boulder, CO, USA, Jun. 2014. [Online]. Available: http:// www.nist.gov/pml/electromagnetics/related-software.cfm.

[24] J. A. Jargon, D. F. Williams, and P. D. Hale, "Developing models for type-N coaxial VNA calibration kits within the NIST Microwave Uncertainty Framework," in *Proc. 87th Autom. Radio Freq. Techn. Group Microw. Meas. Conf.*, 2016, pp. 1–4.

[25] P. Manurkar et al., "Two-Tier Vector-Network-Analyzer Calibrations for Uncertainties in Laboratory-Based Over-the-Air and Channel Measurements," in IEEE Open Journal of Instrumentation and Measurement, vol. 4, pp. 1-17, 2025, Art no. 8000717, doi: 10.1109/OJIM.2025.3619249.

[26] R.J. Mailloux, "Phased Array Antenna Handbook, 3rd ed.," Artech House, 2017.

[27] D. Brown and Y. Rahmat-Samii, "Error vector magnitude as a performance standard for antennas in the millimeter-wave era, part 1: metric comparisons and measurement concepts," *IEEE Ant. and Propagat. Mag.*, Oct. 30, 2023, pp. 25-34.